NASA Technical Memorandum 88944
AIAA-87-0738

Analytical Flutter Investigation of a Composite Propfan Model

K.R.V. Kaza and O. Mehmed
Lewis Research Center
Cleveland, Ohio

G.V. Narayanan
Sverdrup Technology, Inc.
Lewis Research Center
Cleveland, Ohio

D.V. Murthy
The University of Toledo
Toledo, Ohio

Prepared for the
28th Structures, Structural Dynamics, and Materials Conference
cosponsored by the AIAA, ASME, AHS, and ASEE
Monterey, California, April 6–8, 1987

NASA

ANALYTICAL FLUTTER INVESTIGATION OF A COMPOSITE PROPFAN MODEL

K.R.V. Kaza* and O. Mehmed**
National Aeronautics and Space Administration
Lewis Research Center
Cleveland, Ohio 44135

and

G.V. Narayanan
Sverdrup Technology, Inc.
Lewis Research Center
Cleveland, Ohio 44135

and

D.V. Murthy†
The University of Toledo
Toledo, Ohio 43606

E-3392

ABSTRACT

This paper presents a theoretical model and an associated computer program for predicting subsonic bending-torsion flutter in propfans. The model is based on two-dimensional unsteady cascade strip theory and three-dimensional steady and unsteady lifting surface aerodynamic theory in conjunction with a finite element structural model for the blade. The analytical results compare well with published experimental data. Additional parametric studies are also presented illustrating the effects on flutter speed of steady aeroelastic deformations, blade setting angle, rotational speed, number of blades, structural damping, and number of modes.

NOMENCLATURE

a	elastic axis location
[A]	generalized aerodynamic matrix
$A_1, A_2, \ldots, A_m$	torsion contributions of the m normal modes about the reference axis
b	blade semi-chord
{F(t)}	nonaerodynamic nodal force vector
$\{F_0\}$	time-independent nonaerodynamic force vector
f_j	modal frequency of j-th mode in Hz
{G}	generalized motion independent force vector
h	bending deflection
i	$\sqrt{-1}$
j	mode index, j = 1, 2, 3,...
k	reduced frequency ($\omega b/V$)
$[K_g]$	generalized stiffness matrix
$[K_s]$	centrifugal softening matrix in physical coordinates
$[K(\{u\})]$	nonlinear stiffness matrix in physical coordinates
$l_{11}, l_{12}, \ldots l_{26}$	aerodynamic coefficients defined in Eq. (12)
$l_{hh}, l_{h\alpha}\ldots$	aerodynamic coefficients defined in Ref. 13
L	aerodynamic lift
M_a	aerodynamic moment
M	Mach number
[M]	physical mass matrix
$[M_g]$	generalized mass matrix
N	number of blades
[P]	stiffness matrix defined in Eq. (10)
$\{P(\{u\},t)\}$	aerodynamic nodal force vector
$\{P(\{u_0\})\}$	steady-state aerodynamic nodal force vector
{q}	vector of generalized coordinates
$\{q_0\}$	amplitude of motion in generalized coordinates
{Q}	generalized aerodynamic force vector
r	interblade phase angle index, r = 1, 2,..., N; also distance from the axis of rotation
s	blade length along the reference line
t	time
{u}	vector of blade deflections at grid points

*Associate Fellow, AIAA.
**Member AIAA, ASME.
†NASA Resident Research Associate.

$\{u_0\}$	vector of steady state deflections at grid points
$\{u_{0l}\}$	steady state deflections due to centrifugal loads
$\{u_{0i}\}$	steady state deflections after the i-th iteration
V	free stream velocity
V_R	relative velocity
[W]	modal matrix expressed in terms of individual bending and torsion contributions about the reference axis
$W_1, W_2, \ldots, W_m$	bending contributions of m normal modes of the reference axis
XYZ	global coordinate system
$X_1Y_1Z_1$	blade fixed coordinate system
α	torsional deflection
$\beta_{0.75R}$	blade pitch angle at three-quarter radius
γ	eigenvalue defined in Eq. (10)
$\{\Delta F(t)\}$	perturbation nonaerodynamic nodal force vector
$\{\Delta P^W(t)\}$	perturbation aerodynamic nodal force vector (motion-independent)
$\{\Delta P(\{\Delta u\},t)\}$	perturbation aerodynamic nodal force vector (motion-dependent)
$\{\Delta u(t)\}$	vector of vibratory deflections at grid points measured relative to $\{u_0\}$
ζ_j	structural damping ratio in j-th mode
Λ	sweep angle
μ	real part of $i\sqrt{\gamma}$ (proportional to damping)
ν	imaginary part of $i\sqrt{\gamma}$ (flutter frequency)
ρ	density of air
σ_r	interblade phase angle
$[\Phi]$	modal matrix
ω	frequency
ω_j	frequency of j-th mode
Ω	rotational speed

Subscripts

0	steady state value
g	generalized (modal)
F	values at flutter point

Superscripts

.	differentiation with respect to time
T	transpose
'	differentiation with respect to spatial coordinate

INTRODUCTION

The major goals of propfan designs are to maximize aerodynamic efficiency, minimize noise and assure structural integrity. The aerodynamic and acoustic requirements of propfans have resulted in designs with thin, swept, and twisted blades of low aspect ratio and high solidity compared to conventional propellers. These blades operate in subsonic, transonic, and possibly supersonic flows. Furthermore, propfans may have a single rotor with blades rotating in one direction or two rotors rotating in opposite directions. The former is called a single rotation, SR, propfan and the latter is called a counter rotation, CR, propfan.

The unconventional features of the SR propfan add complexity to understanding the aeroelastic phenomena involved and to developing an analytical aeroelastic model. Since the blades are thin and flexible, deflections due to centrifugal and aerodynamic loads are large. Hence, the aeroelastic problem is inherently nonlinear, requiring geometric nonlinear theory of elasticity. Also, the blades are of low aspect ratio with large sweep and, hence, require three-dimensional steady and unsteady aerodynamic models for accurate analysis. The blades have large sweep and twist, which couples blade bending and torsional motions, and are plate-like structures because of their low aspect ratio. These factors require a finite element structural model which accounts for centrifugal softening and stiffening effects and possibly for Coriolis effects. The centrifugal softening terms are important because of large blade sweep and flexibility. The propfan rotor has four or more blades which necessitate the inclusion of aerodynamic coupling or cascade effects between the blades. The flexibility of the hub introduces additional structural coupling between the blades of a rotor. Furthermore, the aerodynamic and structural properties of the individual blades may differ from each other. The presence of these differences requires explicit consideration of both structural and aerodynamic mistuning in the analytical aeroelastic model. Additionally, for the CR propfan, there is aerodynamic interaction between the blades of the two rotors. Because of these unique features of both the SR and CR concepts, it is not possible to directly use the existing aeroelastic technology of conventional propellers or of conventional turbofans or of helicopters.

As a part of the overall NASA single rotation propfan technology program, a series of 0.61 m (2 ft) diameter geometrically scaled models were tested in wind tunnels and on a NASA acoustic research aircraft. The tests and results are summarized in Ref. 1. The published literature on the CR concept is very limited. However, the benefits of the CR concept are discussed in Ref. 2.

The present paper addresses the aeroelastic aspects of the SR propfan only.

Classical flutter of a SR propfan occurred unexpectedly during a previous wind tunnel performance experiment on a model (designated SR-5) with ten highly swept titanium blades. Reference 3 presented experimental data of the SR-5 model and correlated the data with theory. In Ref. 3, the aerodynamic model is based on two-dimensional unsteady cascade theory with a correction for blade sweep and the structural model is an idealized swept beam for each blade. References 4 and 5 refined the analytical model of Ref. 3 by using blade normal modes calculated from a finite-element plate model for the blade, and correlated the refined analytical results with the data of the SR-5 model. The correlation between theory and experiment in Refs. 3 to 5 varied from poor to good.

Additional subsonic wind tunnel flutter data, obtained by testing a composite propfan model, SR3C-X2 (Fig.1), were presented in Ref. 6. A three-dimensional steady and unsteady aerodynamic theory for propfans with subsonic leading edge was presented in Ref. 7, and the theory was applied for predicting flutter for one test case of the wind tunnel model of Ref. 6.

The specific objectives of the present investigation are: (1) to develop a modal flutter analysis method which uses both two-dimensional and three-dimensional steady and unsteady aerodynamics; (2) to conduct parametric studies to ascertain the effect of steady airloads on frequencies, modes and flutter speed, and the effect of number of blades, blade setting angle and blade structural damping on flutter speed; (3) to validate analytical models by correlating analytical and measured flutter speeds of the SR3C-X2 propfan model; and (4) to examine the limitations of two-dimensional unsteady aerodynamic theory for propfan flutter analysis. To accomplish the objectives, a computer program ASTROP (Aeroelastic Stability and Response of Propulsion Systems) was developed. ASTROP was started with two-dimensional unsteady aerodynamic theory corrected for blade sweep. This version is designated ASTROP2. Subsequently, it was enhanced by including three-dimensional steady and unsteady aerodynamics in a version called ASTROP3. ASTROP can use COSMIC NASTRAN[8] or any other finite element code to calculate blade steady state deflections, mode shapes, and frequencies. Presently, COSMIC NASTRAN is used. This paper describes the analytical method and the ASTROP code and presents paremetric results which are believed to be useful for propfan designers and other investigators in the field.

The present work has been extended in Ref. 9 to include the effects of both structural and aerodynamic mistuning on propfan flutter.

ANALYTICAL FORMULATION

The coordinate system used for developing the equation of motion of a rotating propfan blade is shown in Fig. 2. The propfan rotates about the X-axis which is aligned with the freestream direction. The Y-axis is aligned along the blade pitch-axis and the Z-axis is perpendicular to the X-Y plane. Also shown in Fig. 2 are undeflected and deflected positions of an arbitrary blade strip normal to the reference line. The finite-element model of the blade is shown in Fig. 3. The aeroelastic equation of motion of the blade can be written as

$$[M]\{\ddot{u}\} + [K_S]\{u\} + [K(\{u\})]\{u\} = \{P(\{u\},t)\} + \{F(t)\} \qquad (1)$$

where $\{u\}$ represents the blade deflections at the grid points, $[M]$ is the mass matrix, $[K_S]$ the centrifugal softening matrix, $[K(\{u\})]$ the nonlinear stiffness matrix, $\{P(\{u\},t)\}$ the equivalent aerodynamic nodal force vector, and $\{F(t)\}$ the equivalent nonaerodynamic force vector. Because of the large deflections and the consequent need for the geometric nonlinear theory of elasticity in which the strain and displacement relations are nonlinear, the stiffness matrix $[K(\{u\})]$ is a function of nodal displacements and, hence, is nonlinear. The level of the geometric nonlinear theory of elasticity used herein as well as in NASTRAN, is the one in which elongations and shears are negligible compared to unity. This explicit consideration of geometric nonlinear theory of elasticity provides the additional geometric differential stiffness due to centrifugal stiffening terms. The displacement dependent centrifugal softening terms are included in the matrix $[K_S]$, which is linear. The rotation also introduces Coriolis forces, but they are shown to be negligible for thin propfan blades in Ref. 10. Hence, they are not included in the present formulation.

Linearization of Equations

Equation (1) is generally nonlinear and is valid for calculating stalled and unstalled flutter speed, forced response, aeroelastic performance, steady-state deflections, frequencies and mode shapes. An appropriate solution method is to directly integrate in time domain, but it is computationally inefficient. Common practice is to perturb it about a steady-state configuration by writing

$$\left.\begin{aligned} \{u\} &= \{u_0\} + \{\Delta u(t)\} \\ \{P(\{u\},t)\} &= \{P(\{u_0\})\} + \{\Delta P(\{\Delta u\},t)\} + \{\Delta P^W(t)\} \\ \{F(t)\} &= \{F_0\} + \{\Delta F(t)\} \end{aligned}\right\} \qquad (2)$$

where $\{u_0\}$, $\{P(\{u_0\})\}$, and $\{F_0\}$ are the steady state values of $\{u\}$, $\{P(\{u\},t)\}$, and $\{F(t)\}$, respectively. The quantities $\{\Delta u(t)\}$, $\{\Delta P(\{\Delta u\},t)\}$, and $\{\Delta F(t)\}$ are perturbations from $\{u_0\}$, $\{P(\{u_0\})\}$, and $\{Fo\}$, respectively. The perturbation aerodynamic force is split into motion dependent ($\{\Delta P(\{\Delta u\},t)\}$) and motion independent ($\{\Delta P^W(t)\}$) parts for convenience in forced response analysis. Substituting Eq. (2) into the nonlinear Eq. (1) leads to two sets of equations: one steady-state equation for $\{u_0\}$ and another for the perturbation variable $\{\Delta u(t)\}$. These are

$$\left[[K_S] + [K(\{u_0\})]\right]\{u_0\} = \{P(\{u_0\})\} + \{F_0\} \qquad (3)$$

$$[M]\{\Delta\ddot{u}(t)\} + \left[[K_S] + [K(u_0)]\right]\{\Delta u(t)\} = \{\Delta P(\{\Delta u\},t)\} + \{\Delta P^W(t)\} + \{\Delta F(t)\} \qquad (4)$$

Steady-State Configuration and Vibration Analysis

The steady-state configuration for a given rotational speed and Mach number is obtained by solving the nonlinear Eq. (3). The stiffness matrix $[K(\{u_0\})]$ includes elastic stiffness and differential stiffness due to centrifugal stiffening loads and steady-state aerodynamic loads. Once the steady-state deflection and the effective total stiffness are known from Eq. (3), the vibration frequencies and mode shapes are calculated by solving

$$[M]\{\Delta\ddot{u}(t)\} + \left[[K_S] + [K(\{u_0\})]\right]\{\Delta u(t)\} = 0 \qquad (5)$$

which leads to the generalized mass matrix $[M_g]$, the modal matrix $[\Phi]$, and the modal frequencies ω_j.

Flutter and Forced Response by the Modal Method

The general vibratory motion can be expressed as a superposition of the contributions of the various normal modes:

$$\{\Delta u(t)\} = [\Phi]\{q\} \qquad (6)$$

Substituting Eq. (6) into Eq. (4) and post-multiplying the result by $[\Phi]^T$ leads to

$$[M_g]\{\ddot{q}\} + [K_g]\{q\} = [A]\{q\} + \{G(t)\} \qquad (7)$$

where

$$\left.\begin{aligned} [M_g] &= [\Phi]^T [M] [\Phi] \\ K_{gjj} &= M_{gjj}\,\omega_j^2\,(1 + 2i\zeta_j) \\ [A]\{q\} &= [\Phi]^T \{\Delta P(\Delta u, t)\} \\ \{G(t)\} &= [\Phi]^T [\{\Delta F(t)\} + \{\Delta P^W(t)\}] \end{aligned}\right\} \qquad (8)$$

The order of Eq. (7) depends on the number of modes included in Eq. (6). This number is determined by performing numerical experiments, which will be explained later. The structural damping in each mode is introduced through the damping ratio ζ_j where the modal index $j = 1,2,3 \ldots$ The generalized aerodynamic matrix is represented by [A] for each interblade phase angle for simple harmonic motion of the blade. The motion independent aerodynamic and nonaerodynamic forces are represented by $\{G(t)\}$ for each interblade phase angle. This is included for completeness in the formulation, but no results on forced response will be presented in this paper. For simple harmonic motion the flutter eigenvalue problem can be rewritten from Eq. (7) after setting $\{G(t)\} = \{0\}$ as

$$[P]\{q_0\} = \gamma [M_g]\{q_0\} \qquad (9)$$

where

$$\left.\begin{aligned} \{q\} &= \{q_0\}\, e^{i\omega t} \\ [P] &= [K_g] - [A] \\ i\sqrt{\gamma} &= i\omega = \mu + i\nu \end{aligned}\right\} \qquad (10)$$

Flutter occurs when $\mu > 0$.

ASTROP COMPUTER CODE

The ASTROP code is based on the normal mode method and is for flutter, forced response, and whirl flutter analysis of propulsion systems. Only the flutter part of the code that uses two-dimensional subsonic unsteady aerodynamics (ASTROP2) and three-dimensional subsonic steady and unsteady aerodynamics (ASTROP3) are used in the present investigation. Both versions of the code are written in FORTRAN. Data transfer between NASTRAN and aerodynamic codes in ASTROP is made through interfacing subroutines. This code is operational on a CRAY-XMP computer.

ASTROP2

The input to ASTROP2 and the steps involved for solving the flutter problem are shown in the form of a flow chart in Fig. 4. The input consists of blade geometry described by the grid point coordinates in the XYZ system (Fig. 2) and the modal information--frequencies, mode shapes, and generalized masses. For calculating modal information, the equivalent anisotropic material properties for each element are generated by using a preprocessor code COBSTRAN (Ref. 11). The main step, which is No. 3 in Fig. 4, is the calculation of the generalized aerodynamic matrix [A] by using normal modes and an aerodynamic strip representation of the blade. The blade is divided into a series of discrete aerodynamic strips of constant properties, and one of these strips is shown in Fig. 2. Each swept strip has two motions, plunging and pitching about an arbitrary reference line. The lift and moment equations for each section are obtained by extending the unsteady equations for a swept wing generated in Ref. 12 to a linear cascade case. This extension was implemented for the first time in Ref. 3. The lift and moment expressions per unit span are

$$\begin{Bmatrix} L \\ M_a \end{Bmatrix} = \pi\rho\omega^2 \begin{bmatrix} l_{11} & l_{12} & \cdots & l_{16} \\ l_{21} & l_{22} & \cdots & l_{26} \end{bmatrix} \begin{Bmatrix} h \\ \alpha \\ h' \\ \alpha' \\ h'' \\ \alpha'' \end{Bmatrix} \qquad (11)$$

$$l_{11} = l_{hh}b^2 \; ; \; l_{12} = l_{h\alpha}b^3$$

$$l_{13} = \frac{-i}{k} \tan \Lambda \, (1 + l_{hh})b^3$$

$$l_{14} = b^4 \tan \Lambda \left[-\frac{1}{k^2} + \frac{i}{k} \left[\left(\frac{1}{2} + a\right) - \left(\frac{1}{2} - a\right) l_{hh} \right] \right]$$

$$l_{15} = \frac{-b^4}{k^2} \tan^2 \Lambda$$

$$l_{16} = \frac{b^5 \, a \tan^2 \Lambda}{k^2} \qquad (12)$$

$$l_{21} = b^3 l_{\alpha h} \; ; \; l_{22} = b^4 l_{\alpha\alpha}$$

$$l_{23} = \frac{b^4 i}{k} \tan \lambda (a - l_{\alpha h})$$

$$l_{24} = \frac{b^5 i \tan \Lambda}{k} \left[\frac{-3}{8} - \left(\frac{1}{8} + a^2\right) + \frac{i}{k}\left(\frac{1}{2} - a\right) + \left(\frac{1}{4} - a^2\right) l_{hh} \right]$$

$$l_{25} = \frac{b^5 a}{k^2} \tan^2 \Lambda$$

$$l_{26} = \frac{-b^6}{k^2} \tan^2 \Lambda \left(\frac{1}{8} + a^2\right)$$

The definitions of the unsteady coefficients l_{hh}, $l_{h\alpha}$, etc. are the same as those in Ref. 13 and these are calculated by using the theory presented in Ref. 14 for each interblade phase angle. For each strip the quantities h and α are expressed in terms of normal modes and normal coordinates, and the gap-to-chord ratio, sweep angle, and stagger angle are calculated from the steady-state configuration.

The effective Mach number for each strip is obtained from the relative velocity and the sweep angle. Then, the generalized aerodynamic force vector can be expressed in terms of lift, moment, normal modes, and normal coordinates as

$$\{Q\} = \pi\rho\omega^2 \int_0^s [W]^T [L] \begin{Bmatrix} [W] \\ [W'] \\ [W''] \end{Bmatrix} \{q\} = [A] \{q\} \qquad (13)$$

where

$$[W] = \begin{bmatrix} W_1 & W_2 & \cdots & W_m \\ A_1 & A_2 & \cdots & A_m \end{bmatrix}$$

$$\begin{Bmatrix} h \\ \alpha \end{Bmatrix} = [W] \{q\} \qquad (14)$$

The coefficients of the matrix [A] in Eq. (13) are obtained by numerical integration using Gaussian Quadrature. The user can choose either the undeflected blade position or the deflected position due to centrifugal loads to calculate blade properties such as stagger, sweep, and gap-to-chord ratio for each strip.

Then the flutter problem described in Eq. (10) is solved in step 4 of Fig. 4. Then, steps 2 to 4 are repeated until the conditions in steps 5 and 6 are met. Finally, the critical flutter variables are extracted in step 7. The main limitations of the analytical model used in the code are: (1) the validity of aerodynamic strip theory for propfans; (2) the validity of the sweep correction in the presence of cascade effects; (3) the arbitrariness of the reference line; and (4) the approximation involved in calculating α and its derivatives along the reference line from the normal modes.

ASTROP3

This version of the code consists of three branches. The blade steady-state pressures, generalized unsteady aerodynamic forces and stability, and forced response due to yawed-flow are calculated in branches one, two, and three, respectively. Only the first two branches are shown in the form of a flow chart in Fig. 5 because forced response is not addressed in the present paper. This is an expanded and modified version of the code described in Ref. 7. The structural model is again based on a finite element approximation. The aerodynamic analysis is based on three-dimensional subsonic compressible lifting surface theory in which blade stall and transonic shock waves are not included.

The input to ASTROP3 and the solution procedure are almost the same as those for ASTROP2. However, the effect of steady three-dimensional airloads is included in calculating the steady-state configuration and the differential stiffness in steps 3 to 6 of Fig. 5. This feature also provides the steady aeroelastic performance at each iteration of the nonlinear solution of Eq. (3). The performance results can be printed in step 6 of Fig. 5.

The iterative-interaction process, steps 4 to 6, is continued until the deflection from the $(i + 1)^{th}$ iteration is equal to that from the i th iteration. Then, the frequencies and mode shapes are calculated in step 7.

The generalized aerodynamic coefficient matrix, A, is calculated in step 9 by using the procedure outlined in Ref. 7. The eigenvalue problem in step 10 is repeated until the flutter conditions in steps 11 and 12 are met. The entire procedure is repeated for each interblade phase angle and the critical flutter variables are printed in step 13.

RESULTS AND DISCUSSION

The propfan flutter research model, Fig. 1, SR3C-X2, is analyzed. The blades are made from graphite-ply/epoxy-matrix material. There are eight blades on the propfan. The geometric mid-chord sweep is 45° at the tip and the tip diameter is 0.61 m (2 ft). The blade mass ratio is approximately 33. The model has been tested for flutter at various rotational speeds, freestream Mach numbers, and blade setting angles. Details on the model and flutter data can be found in Ref. 6.

The finite element model of the blade (Fig. 3) consists of 228 grid points and 388 plate elements. The hub of the blades is assumed rigid and is not modeled. Also, all the blades are assumed to be aerodynamically, geometrically, and structurally identical. Consequently, it is adequate to model one blade and to analyze each interblade phase angle independently. The effects of nonidentical blade properties are addressed in Ref. 9.

Frequencies and Mode Shapes

Figure 6 shows the variation of the SR3C-X2 blade natural frequencies with rotational speed in vacuum. The measured bench natural frequency band of the eight blades is shown for comparison. The frequencies are calculated with centrifugal loads (CL) for all rotational speeds and with centrifugal loads and steady three-dimensional airloads (CL + AL) at 6100 rpm by the procedure described in Fig. 5 (steps 1 to 7). Figure 7 shows hologram photos of the measured modes and the corresponding calculated modes. The holograms for only the first two modes are included because it will be shown later that the flutter mode is a combination of the first two modes. The fringes represent constant displacement contours, the whitest ones being nodes. It can be seen from the figure that the measured and calculated frequencies for the first mode correlate but the measured frequencies for the second to 4th mode are lower than the calculated ones. Also, the steady airloads do not have significant effect on the frequencies. The first mode frequency increases with an increase in rotational speed. This trend is expected because of centrifugal stiffening. The second and third mode frequencies do not change significantly with rotational speed. It can be seen from the contour plots that the first mode is primarily flexural but also has a large degree of torsion and the second mode is primarily torsion near the tip. The correlation between theory and experiment for the first two modes is reasonably good and for the higher modes the correlation is poor. The difference between the average measured (375 Hz) and the calculated frequency (399 Hz) for the second mode is attributed to the modeling of the composites and/or to root effects. Even though the effect of aerodynamic loads on frequencies is small, its effect on deflection, particularly at the tip, is appreciable in some cases and will be discussed later.

Effect of Centrifugal Loads and Steady Airloads on Blade Steady State Configuration

Figure 8 shows the variation of the blade steady-state pitch angle at the three-quarter radius with iteration number from the nonlinear aeroelastic analysis with rotational speed and Mach number as parameters. The nonlinear analysis procedure described in Fig. 5, steps 1 to 6 is used. The blade angle for iteration '0' corresponds to the undeflected position (UP); for iteration '1' the steady state configuration with centrifugal loads (CL); for iteration '2' the blade steady-state configuration with centrifugal loads and the aerodynamic loads on the configuration obtained in iteration '1'; for iteration '3' the steady state configuration with centrifugal loads and aerodynamic loads on the configuration from iteration '2'; and so on. It can be seen from the figure that the centrifugal loads untwist the blades and this untwist increases with rotational speed. The untwist angle at 0.75R for 7400 rpm is approximately 2°. The aerodynamic loads also untwist the blade and contribute an additional untwist at 0.75R for 7400 rpm and M = 0.5 of approximately 0.65°. The convergence with both centrifugal and aerodynamic loads is accomplished with five iterations. In other words the aerodynamic loads have to be updated at least four times in the analysis. The converged position is designated by CL + AL. In addition to blade pitch angle change, there is a change in blade camber, particularly at the blade tip. These changes have a very significant effect on blade performance, as well as, on flutter; and the effect is expected to be even more significant in transonic flows. Thus, one should include steady air loads in performance, flutter and forced response analysis of propfans.

Effect of Unsteady Cascade Aerodynamics on Blade Flutter

To illustrate the effect of cascade aerodynamics on flutter, the real and imaginary parts of the eigenvalues of the critical flutter mode of the SR3C-X2 wind tunnel model are shown in Fig. 9. These results are obtained by using the procedure described in Fig. 5 steps 1 to 13 without steady airloads. After calculating the critical freestream Mach number and the critical interblade phase angle, the eigenvalues for other interblade phase angles are calculated. Since there are eight interblade phase angles, $\sigma_r = 360r/8$ where the phase index r = 0,1,. . . 7, Fig. 9 may be interpreted as a root locus of the interblade phase angle modes. For comparison the root loci for the four blade configuration and for the single blade case are also included in Fig. 9. Because of the aerodynamic interaction (cascade effect) between the blades, the single point splits into 4 and 8 for the four and eight blade cases, respectively. When these points are joined, a rough ellipse is formed for each case. The destabilizing influence of the cascade effect is indicated by the length of the semi-major axis of the ellipse. The results clearly show that the cascade effect is very significant even for the case of four blades. This is confirmed by the experiment as will be shown in the later results. The other point to be noted from this figure is that the most critical flutter interblade phase angle for the eight blade case is 225°, which is a three nodal diameter backward traveling wave in the notation employed herein, and that for the four blade case it is 180°.

Effect of Freestream Mach Number on Effective Damping

Figure 10 shows the variation of the real part of the eigenvalue with freestream Mach number at Ω = 6080 rpm, $\beta_{0.75R} = 61.6°$, and $\sigma_r = 225°$. The real part of the eigenvalue is proportional to modal damping. The real part of the eigenvalue is plotted for the critical flutter mode only. For the case of no structural damping, $\zeta = 0$, the real part of the eigenvalue is almost constant for Mach numbers between 0.3 and 0.4 and starts increasing rapidly for M between 0.4 and 0.6.

Effect of Structural Damping

As mentioned earlier, structural damping is introduced into the analysis, Eq. (8), through the viscous damping ratio. The effect of structural

damping on the real part of the eigenvalues is also included in Fig. 10. It can be seen from the figure that a damping ratio of 0.02 in each mode has increased the flutter Mach number from 0.595 to 0.615. Also, the results show that a structural damping ratio of 0.04 in each mode increases the effective damping ratio only to 0.024 for the critical mode. Thus the effective damping is not increased by the full amount of the added structural damping. The effective damping ratio is the ratio of the real and imaginary parts of the eigenvalue. The value of the damping ratio for composite blades of the SR3C-X2 model is of the order of 0.02. Since the value of ζ and the consequent increase in flutter Mach number for the SR3C-X2 blades are small, all the analytical predictions in this paper are made with $\zeta = 0$. Consequently, the analytical results are slightly conservative.

Comparison of Calculated and Measured Flutter Boundary

The calculated flutter boundaries for various steady state configurations and for various perturbation cases are compared with measured boundaries in Figs. 11 and 12 for 8 and 4 blade cases, respectively. The flutter boundary is shown as a variation of freestream Mach number with rotational speed with blade pitch angle as a parameter. Three blade pitch angles 61.6°, 56.6°, and 68.4° are considered for comparison. The steady state configurations that might be used in various degrees of approximation are: (1) undeflected position, UP, (2) deflected position with centrifugal loads, CL; and (3) deflected position with centrifugal and three-dimensional steady airloads, CL + AL. The possible perturbation cases are designated by modes and frequencies and these are: (1) with centrifugal loads, CL; (2) with centrifugal loads and corrected second mode frequency, CL and f_2 = 375 Hz; (3) with centrifugal loads and three-dimensional airloads, CL + AL; and (4) same as three with f_2 = 375 Hz. The case with f(2) = 375 Hz is included because the measured nonrotating frequency for the second mode is 375 Hz and the calculated value is 399 Hz. Since this frequency, as shown by theory, Fig. 6, is independent of rotational speed, the measured value is used in flutter speed calculations. To minimize computational time, all these possible configurations are considered only for $\beta_{0.75R} = 61.6°$.

Correlation of calculated and measured flutter Mach numbers. - Comparing the calculated Mach numbers for the case in which the UP as the steady state and the CL as the perturbation state with the measured ones in Fig. 11(a) for $\beta_{0.75R} = 61.6°$, the correlation between theory and experiment is very good for Ω = 5280 and 6080 rpm. However, the calculated Mach number for Ω = 7320 rpm is slightly higher than the measured value. A similar comparison with the same steady and perturbation states in Fig. 11(b) for $\beta_{0.75R} = 56.6°$ and in Fig. 11(c) for $\beta_{0.75R} = 68.4°$ also shows very good agreement between theory and experiment. The predicted slope of the flutter boundary line for all the blade pitch angles agrees well with that of the experiment. Both theory and experiment show that for a given rpm the freestream flutter Mach number decreases with an increase in the blade pitch angle. For example, when Ω = 6000 rpm, the flutter Mach number is 0.62 for a blade pitch angle is 56.6° (Fig. 11(b)), and is 0.6 for a pitch angle is 61.6° (Fig. 11(a)).

The comparisons made in Fig. 11 for the eight-blade case with the steady state UP and the perturbation state CL are repeated in Fig. 12 for the four-blade case. As can be seen, the correlation between theory and experiment again is very good. However, the difference between the calculated and measured flutter Mach numbers for the four-blade case is slightly greater. It implies that the theory may be overcorrecting for the aerodynamic cascade effects for the four-blade case.

Effect of change in steady state configuration due to centrifugal loads. - Calculated flutter Mach numbers with the steady state UP and the perturbation CL are compared in Figs. 11 and 12 with the corresponding calculated ones with the steady and perturbation states as CL for all the blade pitch angles. It is evident from the results that the change in the steady state from UP to the CL does not have an appreciable effect on flutter Mach numbers.

Sensitivity of flutter Mach number to frequency. - Comparison of calculated flutter Mach numbers with the steady state UP and the perturbation state as CL with corresponding calculated ones with the same steady state and the perturbation state and f_2 = 375 Hz shows that the flutter speed is very sensitive to change in the second mode frequency for all the cases in Figs. 11 and 12. For example, the flutter Mach number is decreased from 0.6 to 0.55 at Ω = 6080 rpm (Fig. 11(a)) when the second mode frequency is reduced from 399 to 375 Hz. Comparing the calculated flutter Mach numbers with the steady state UP and the perturbation state CL, f_2 = 375 Hz with the corresponding measured ones in Figs. 11 and 12, one can infer that the calculated Mach numbers are slightly less than the measured ones for all the blade pitch angles (Figs. 11(b) to (c)) with eight blades and for the blade pitch angle 56.6° (Fig. 12(b)) with four blades. Furthermore, the experimental boundary for these cases lies between the two calculated boundaries. However, when the blade pitch angle is 61.6° with four blades, the experimental boundary agrees well with the calculated one with the steady state UP and the perturbation state CL and f_2 = 375 Hz. Also, as can be seen in Figs. 12(a) and (b), there is a kink in flutter boundary, and the kink was predicted in Fig. 12(b) by taking a smaller step in rotational speed. The precise reason for the kink is not known.

Effect of steady air loads on flutter speed. - Flutter Mach numbers calculated with the CL for both the steady and perturbation states are compared in Fig. 11(a) with the corresponding ones with the CL + AL for both the steady and perturbation states. It is evident from the results that the steady airloads have a significant influence on flutter speed. The influence increases with increasing rotational speed. For example, the increase in predicted Mach number is 0.01 at Ω = 5280 rpm, and 0.02 at Ω = 6080 rpm, and 0.05 at Ω = 7370 rpm. Even though the change in model frequencies due to steady state airloads is small, there is a significant change in blade camber and mode shapes at higher rpm. Thus, the increase in flutter speed at higher rpm due to steady airloads is attributed to (1) small changes in modal frequencies, (2) mode shape changes, and (3) change in blade steady state angle and hence

blade stagger angle. The change in flutter Mach number with steady airloads due to a reduction in second mode frequency from 399 to 375 Hz in Fig. 11(a) is the same as that without steady airloads. The best theoretical boundary in Fig. 11(a) is the one for which CL + AL is the steady state and CL + AL and f_2 = 375 Hz is the perturbation state. Comparing the best boundary with the experimental one, the correlation is very good.

Effect of Number of Modes on Flutter Analysis

The theoretical results presented in Figs. 11 and 12 were obtained by varying the number of modes from 2 to 6 in the perturbation analysis. There is no appreciable effect on flutter speed by increasing the number of modes beyond two. In the other words, the flutter mode is a combination of first and second natural modes and there is very little participation of higher modes.

Correlation of Measured and Calculated Flutter Frequencies

Measured and calculated flutter frequencies for the configurations described in Fig. 11(a) are compared in Fig. 13. In general the calculated flutter frequency is higher than the measured value. The correlation between theory and experiment is better when second mode frequency is corrected to 375 Hz and when steady state aerodynamics are included. Even for this case the calculated flutter frequencies are approximately 7 percent higher than the measured ones. A similar correlation was noticed for other blade setting angles and for four-bladed cases, and they are not shown herein.

Correlation of Measured and Calculated Flutter Interblade Phase Angles

Another important parameter for propfan flutter is the interblade phase angle. The measured and calculated flutter interblade phase angles are shown for the eight bladed case in Fig. 14. The interblade phase angle with respect to blade one is plotted against the blade number. The calculated interblade blade phase angle, Fig. 14(a), for $\beta_{0.75R} = 61.6^\circ$ is 225° which corresponds to a three nodal diameter backward travelling wave. The predominant measured value is also 225°. However, the measured value is slightly off from 225° for some blades. This is possibly caused by the slight frequency mistuning that is present in the rotor. The same type of correlation between theory and experiment was noticed at other rotational speeds and, hence, those results are not shown. However, for blade setting of 56.6°, two interblade phase angles, 180° and 225° are present in the measured flutter mode as shown in Fig. 14(b). The frequencies of the two interblade angle modes are slightly different. Surprisingly, theory also predicted the presence of the two interblade phase angles, and the correlation is extremely good. Furthermore, comparison of Figs. 14(a) and (b) shows that the flutter interblade phase angle is a function of blade setting angle.

For the four bladed rotor the correlation between the measured and calculated interblade phase angles is very good. Here, the predominant interblade phase angle both in experiment and theory is 180° for all blade setting angles and rotational speeds considered in Fig. 12. These results are not shown because of space limitation.

Evaluation of Two-Dimensional Unsteady Aero for Flutter Prediction

To assess the validity of two-dimensional aerodynamic theory and the associated sweep correction, the real part of the eigenvalue of the critical mode calculated by using both two-dimensional and three-dimensional theories are compared in Fig. 15. Also included in this figure is the measured flutter Mach number. In the ASTROP2 code, which uses two-dimensional aerodynamics, the reference line of the blade (Fig. 2(a)) is somewhat arbitrary. Also, the sweep of each strip depends on the reference line. In the present calculations the leading edge is used as reference line. From the results it is evident that two-dimensional theory is less accurate than the three-dimensional theory in predicting flutter Mach number. Correlative studies were also conducted by varying free-stream Mach number, blade sweep, rotational speed, and blade setting angle. The correlation varied from poor to good. In some cases the expected conservative nature of the two-dimensional theory did not prevail, possibly because of the arbitrariness of the reference line and the associated aerodynamic sweep correction. Hence, it is concluded that two-dimensional aero theory is adequate for conducting parametric studies and for initial design flutter calculations, but three-dimensional theory should be used for more accuracy.

CONCLUSIONS

A theoretical model and the associated computer program was developed for predicting subsonic flutter of propfans. Theoretical results were correlated with published measured data. These studies and additional parametric results conducted lead to the following conclusions:

1. In general, the agreement between theory and experiment in predicting flutter speeds and interblade phase angles is very good. However, the predicted flutter frequencies with three-dimensional unsteady aerodynamic theory are slightly higher than the measured ones in all the cases.

2. The flutter speed predicted by two-dimensional aero theory is less accurate than that predicted by three-dimensional theory. It can be used for conducting parametric studies and for initial designs. However, the final design calculations should be done with three-dimensional analysis.

3. The influence of steady-state aerodynamics on the steady-state configuration, mode shapes, and flutter is significant in some cases. Thus, they should be included in the final design calculations.

4. Both theory and experiment showed that increasing the number of blades on the rotor is destabilizing. This is inferred to be due to a difference in cascade effects. Thus, the aerodynamic cascade effects should be included in the analysis when the number of blades is four or more.

5. Both theory and experiment showed that increasing the blade setting angle is stabilizing. This is inferred to be due to a change in blade aerodynamic coupling because of change in blade stagger and a change in blade loading and hence blade frequencies and modes.

6. For the rotor considered, the flutter mode is dominated by the first two blade normal modes and there is strong coupling between the two modes.

7. Both theory and experiment showed that under certain conditions two interblade phase angle modes with slightly different frequencies may be present during flutter. Furthermore, the flutter interblade phase angle is a function of blade setting angle and number of blades on the rotor.

REFERENCES

1. Mikkelson, D.C., Mitchell, G.A., and Bober, L.J., "Summary of Recent NASA Propeller Research," NASA TM-83733, 1984.

2. Strack, W.C. etc., "Technology and Benefits of Aircraft Counter Rotation Propellers," NASA TM-82983, 1981.

3. Mehmed, O., Kaza, K.R.V., Kielb, R.E., and Lubomski, J.F., "Bending-Torsion Flutter of a Highly Swept Advanced Turboprop," NASA TM-82975, 1981.

4. Elchuri, V., and Smith, G.C.C., "Flutter Analysis of Advanced Turbopropellers," AIAA Journal, Vol. 22, No. 6, June 1984, pp. 801-802.

5. Turnburg, J.E., "Classical Flutter Stability of Swept Propellers," AIAA Paper 83-0847, May 1983.

6. Mehmed, O., and Kaza, K.R.V., "Experimental Classical Flutter Results of a Composite Advanced Turboprop Model," NASA TM-88972, 1986.

7. Williams, M.H., and Hwang, C., "Three Dimensional Unsteady Aerodynamics and Aeroelastic Response of Advanced Turboprops," AIAA 27th Structures, Structural Dynamics, and Materials Conference, Part 2, AIAA, New York, 1986, pp. 116-124.

8. The NASTRAN Theoretical Manual, NASA SP-221(06), 1981.

9. Kaza, K.R.V., Williams, M.H., Mehmed, O., and Moss, L.E., "Analytical and Experimental Investigation of Mistuning on Advanced Propfan Flutter," AIAA Paper 87-0739, presented at the AIAA/ASME/ASEE/AHS 28th Structures, Structural Dynamics, and Materials Conference, Monterey, CA, Apr. 6-8, 1987.

10. Subrahmanyam, K.B., and Kaza, K.R.V., Brown, G.V., and Lawrence, C., "Nonlinear Bending-Torsional Vibration and Stability of Rotating, Pretwisted, Preconed Blades Including Coriolis Effects," NASA TM-87207, 1986.

11. Chamis, C.C., "Integrated Analysis of Engine Structures," NASA TM-82713, 1981.

12. Barmby, J.G., Cunningham, H.J., and Garrick, I.E., "Study of Effects of Sweep on the Flutter of Cantilever Wings," NACA TN-2121, 1950.

13. Kaza, K.R.V., and Kielb, R.E., "Flutter and Response of a Mistuned Cascade in Incompressible Flow," AIAA Journal, Vol. 20, No. 8, Aug. 1982, pp. 1120-1127.

14. Rao, B.M., and Jones, W.P., "Unsteady Airloads for a Cascade of Staggered Blades in Subsonic Flow," Unsteady Phenomena in Turbomachinery, AGARD CP-177, AGARD, France, 1976, pp. 32-1 to 32-10.

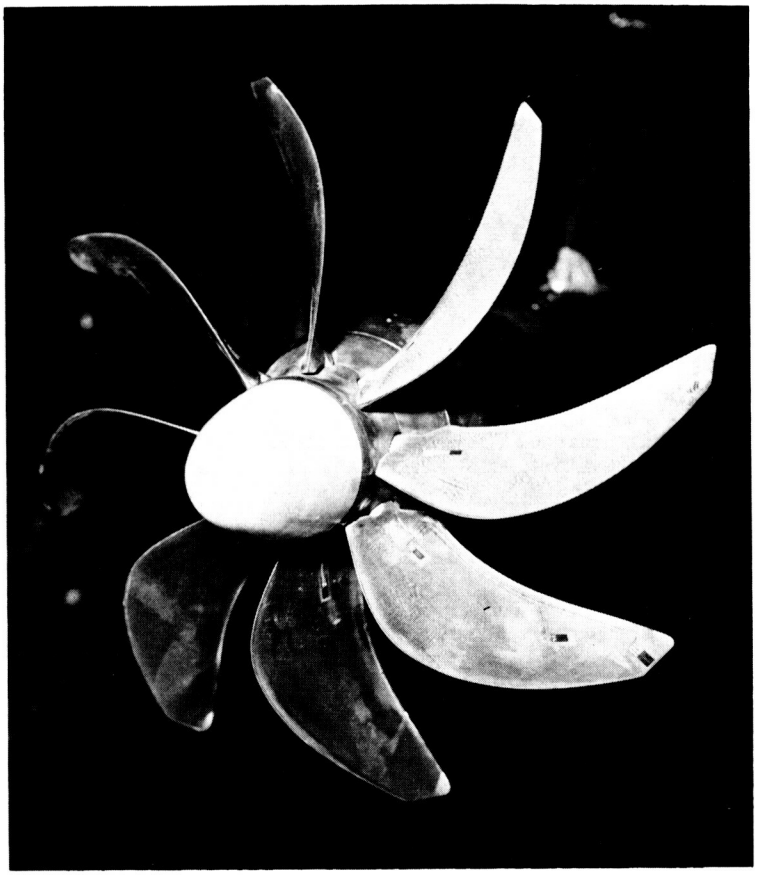

FIGURE 1.- THE SR3C-X2 PROPFAN MODEL IN THE LEWIS 8x6 FT WIND TUNNEL.

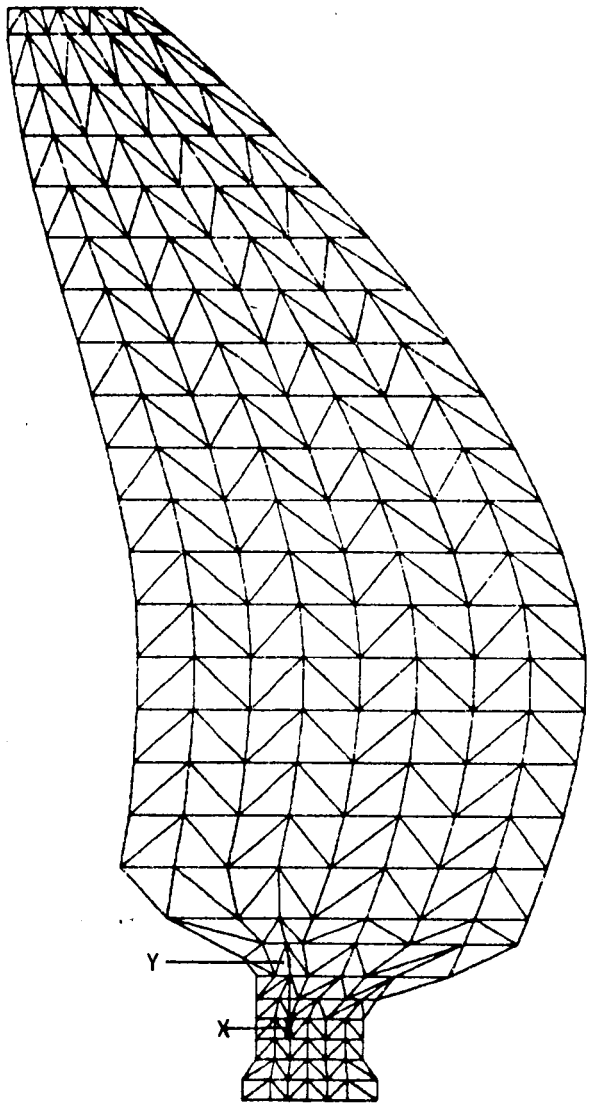

FIGURE 2. - FINITE ELEMENT MODEL OF PROPFAN BLADE.

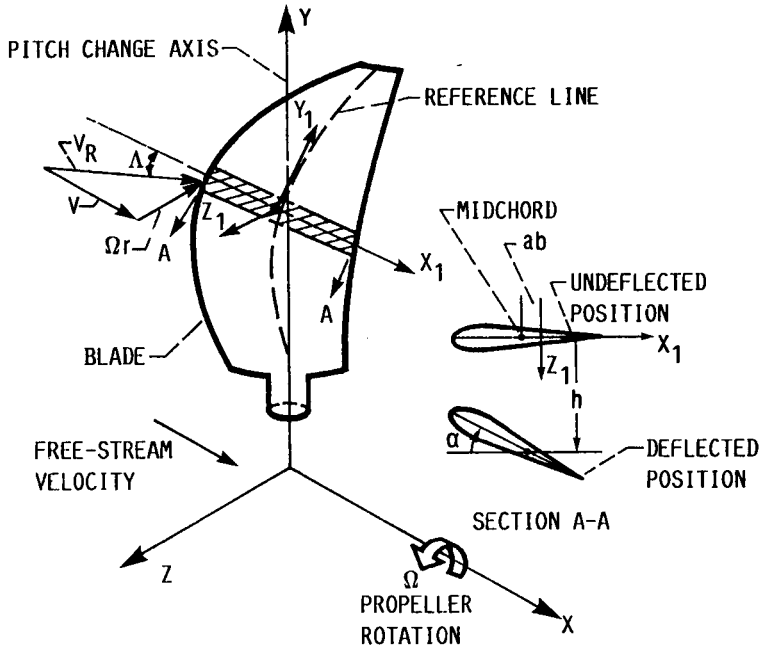

FIGURE 3.- COORDINATE SYSTEM FOR PROPFAN BLADE.

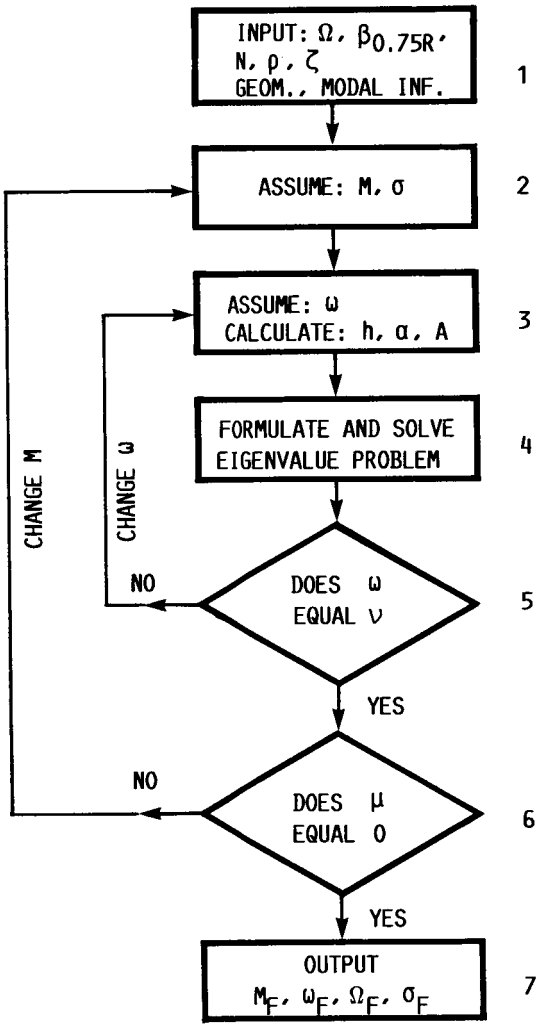

FIGURE 4.- ASTROP2 FLOW CHART.

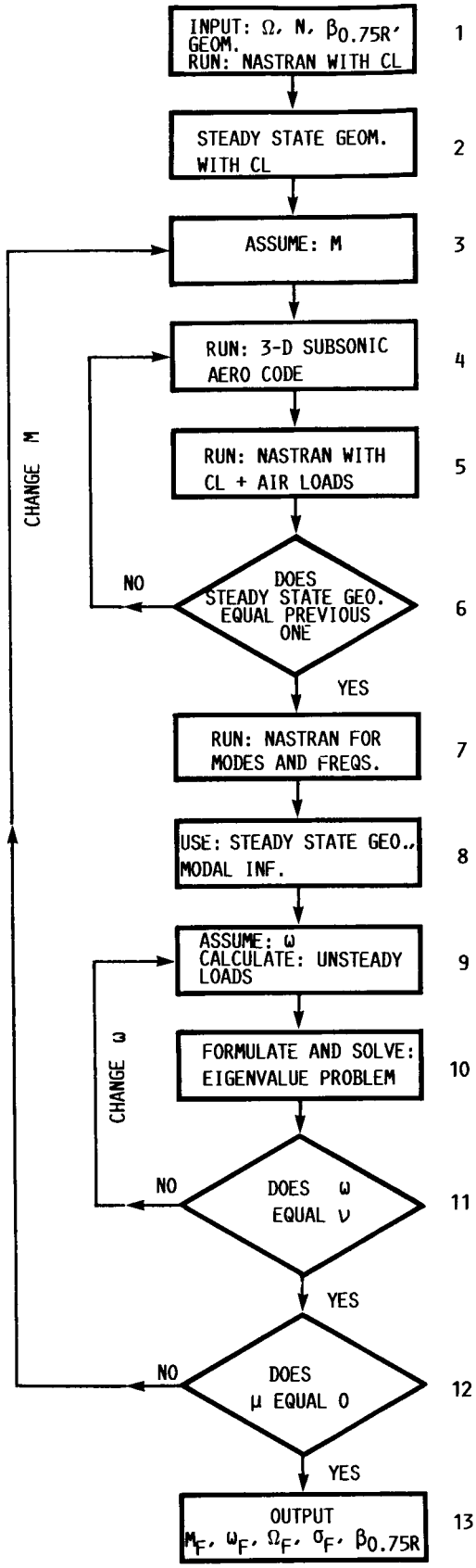

FIGURE 5.- ASTROP3 FLOW CHART.

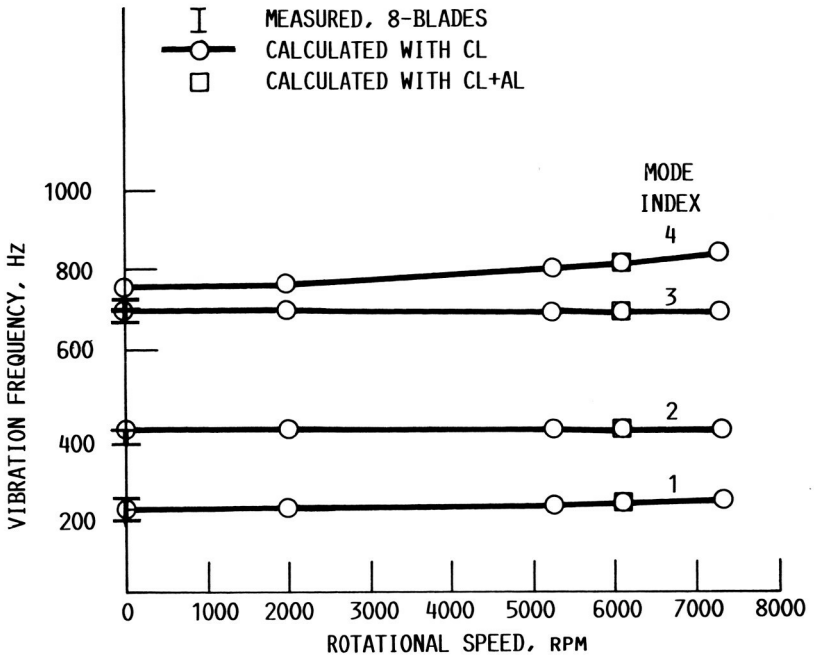

FIGURE 6.- VARIATION OF BLADE NATURAL FREQUENCIES WITH ROTATIONAL SPEED $\beta_{0.75R} = 61.6^{o}$, COSMIC NASTRAN.

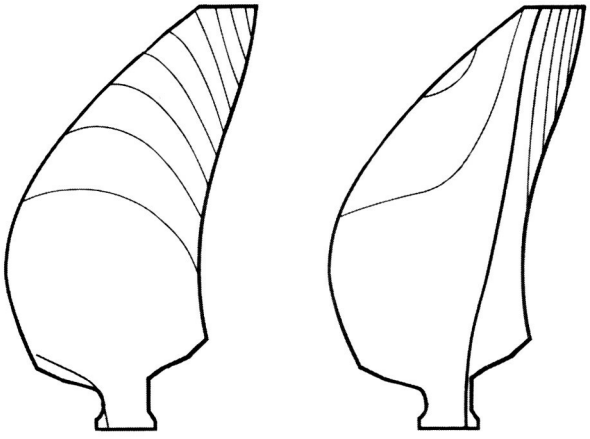

(a) CALCULATED.

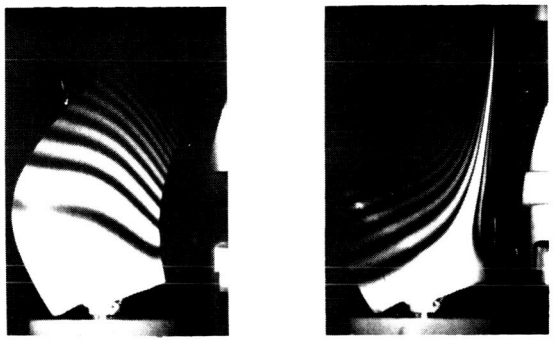

MODE 1 MODE 2

(b) MEASURED, BLADE NO. 6.

FIGURE 7.- COMPARISON OF CALCULATED AND MEASURED MODE SHAPES.

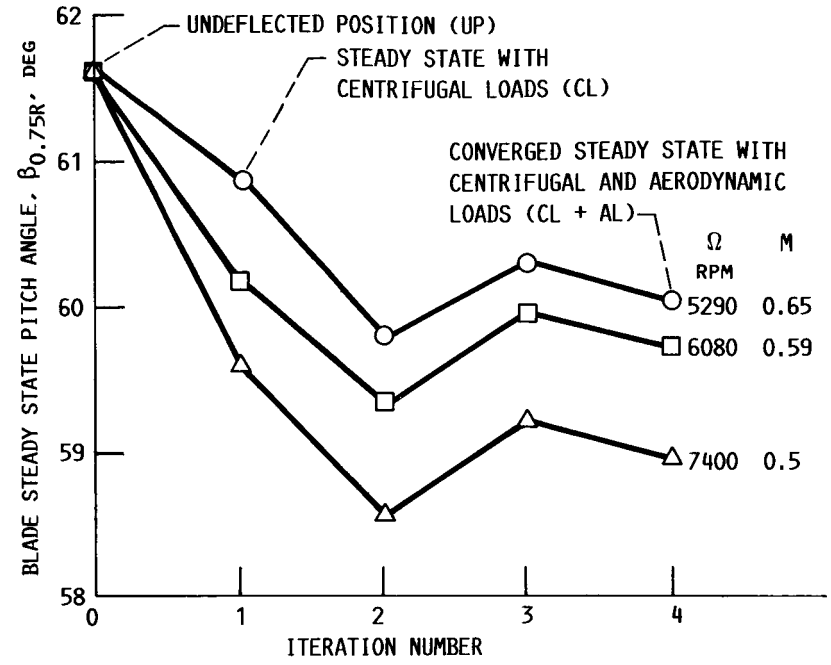

FIGURE 8.- EFFECTS OF CENTRIFUGAL AND AERODYNAMIC LOADS ON BLADE STEADY STATE PITCH ANGLE AT 0.75R.

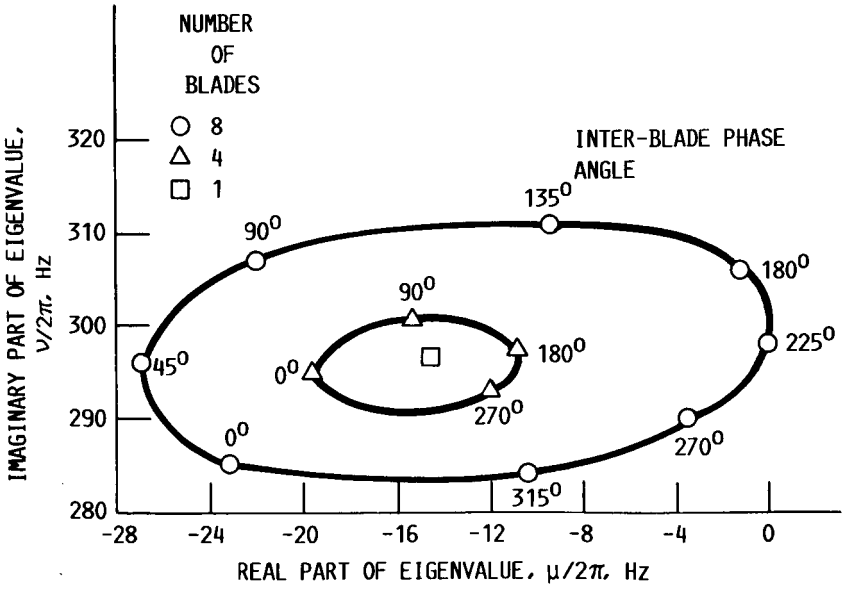

FIGURE 9.- ROOT LOCUS PLOT OF THE MODE WITH LEAST DAMPING: M = 0.59, Ω = 6080 RPM, $\beta_{0.75R} = 61.6^{0}$.

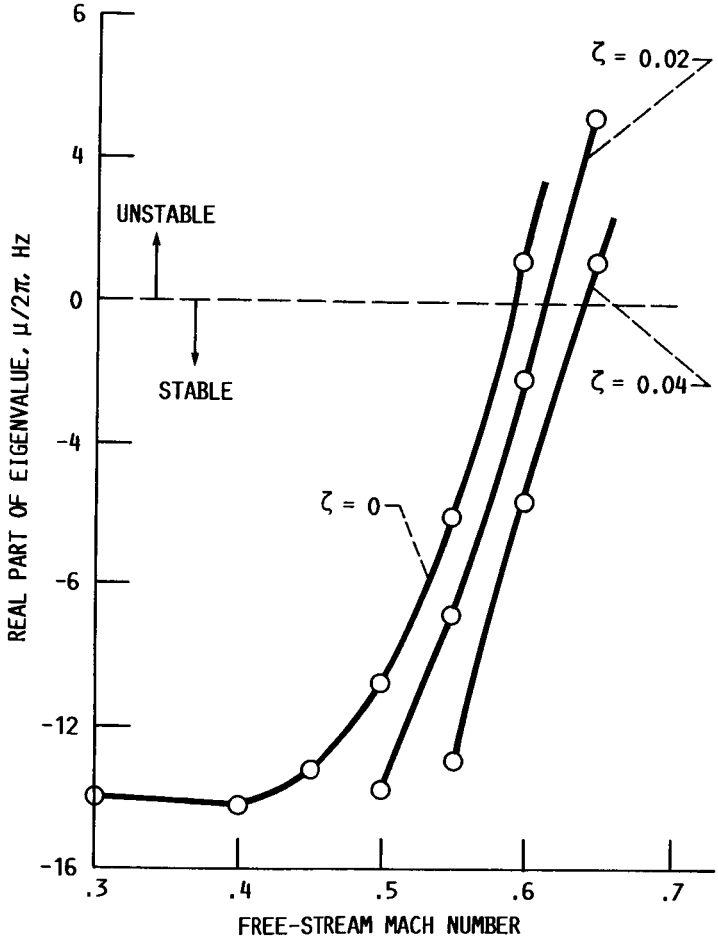

FIGURE 10.- VARIATION OF DAMPING WITH MACH NUMBER: Ω = 6080 RPM, $\beta_{0.75R} = 61.6^{o}$, $\sigma_r = 225^{o}$, N = 8.

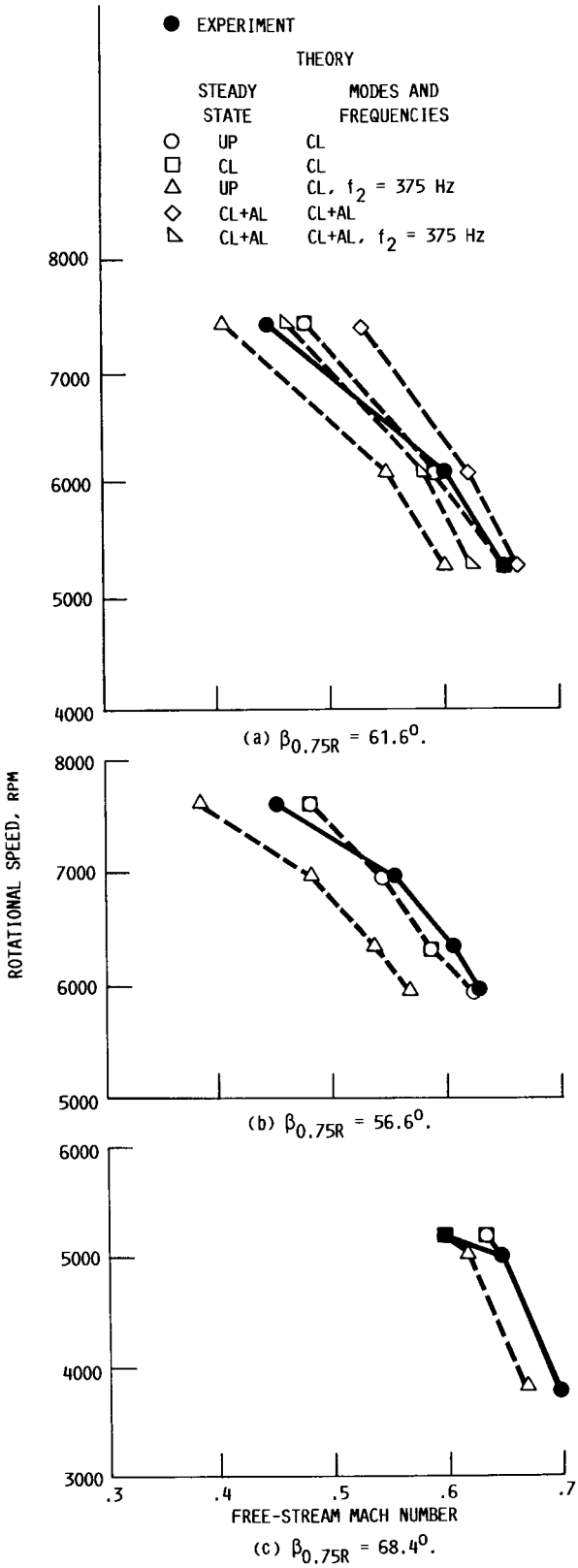

(a) $\beta_{0.75R} = 61.6^{o}$.

(b) $\beta_{0.75R} = 56.6^{o}$.

(c) $\beta_{0.75R} = 68.4^{o}$.

FIGURE 11.- COMPARISON OF MEASURED AND CALCULATED FLUTTER BOUNDARY, 8 BLADES.

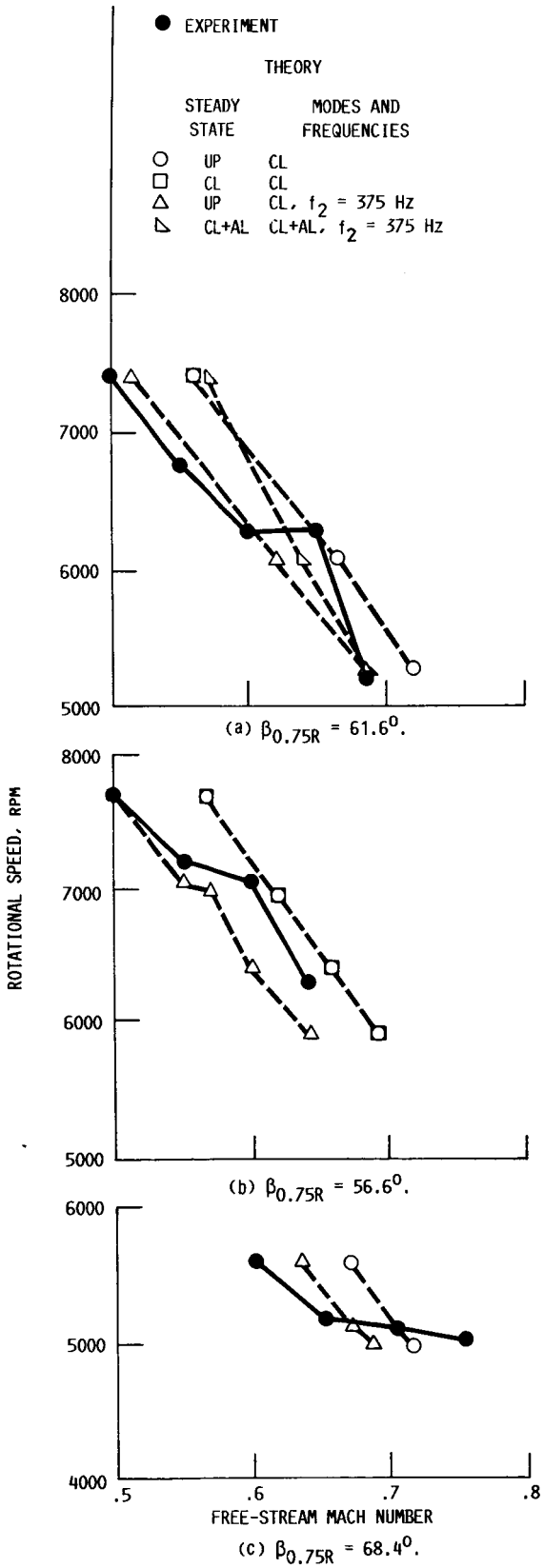

FIGURE 12.- COMPARISON OF MEASURED AND CALCULATED FLUTTER BOUNDARY, 4 BLADES.

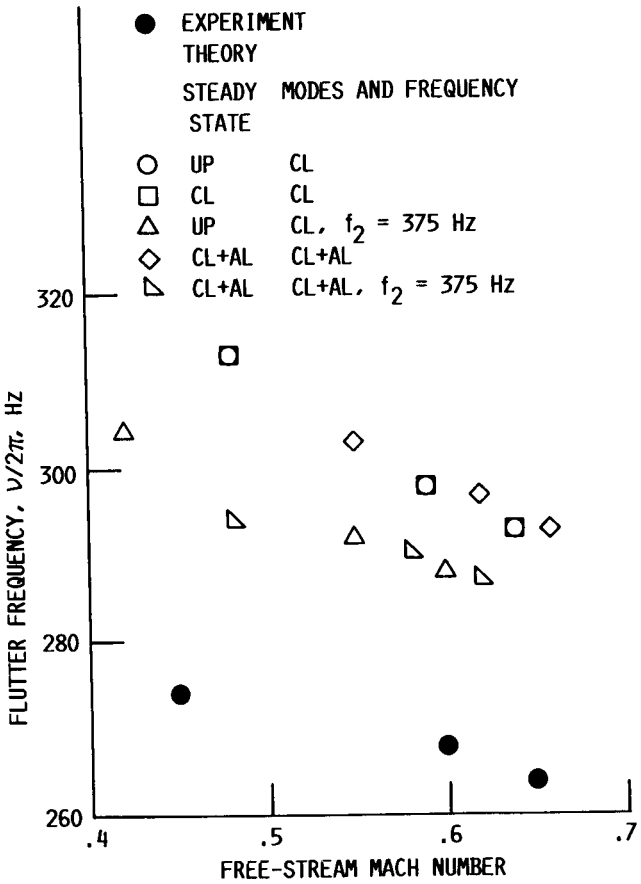

FIGURE 13.- COMPARISON OF MEASURED AND CALCULATED FLUTTER FREQUENCIES, 8 BLADES, $\beta_{0.75R} = 61.6^{o}$.

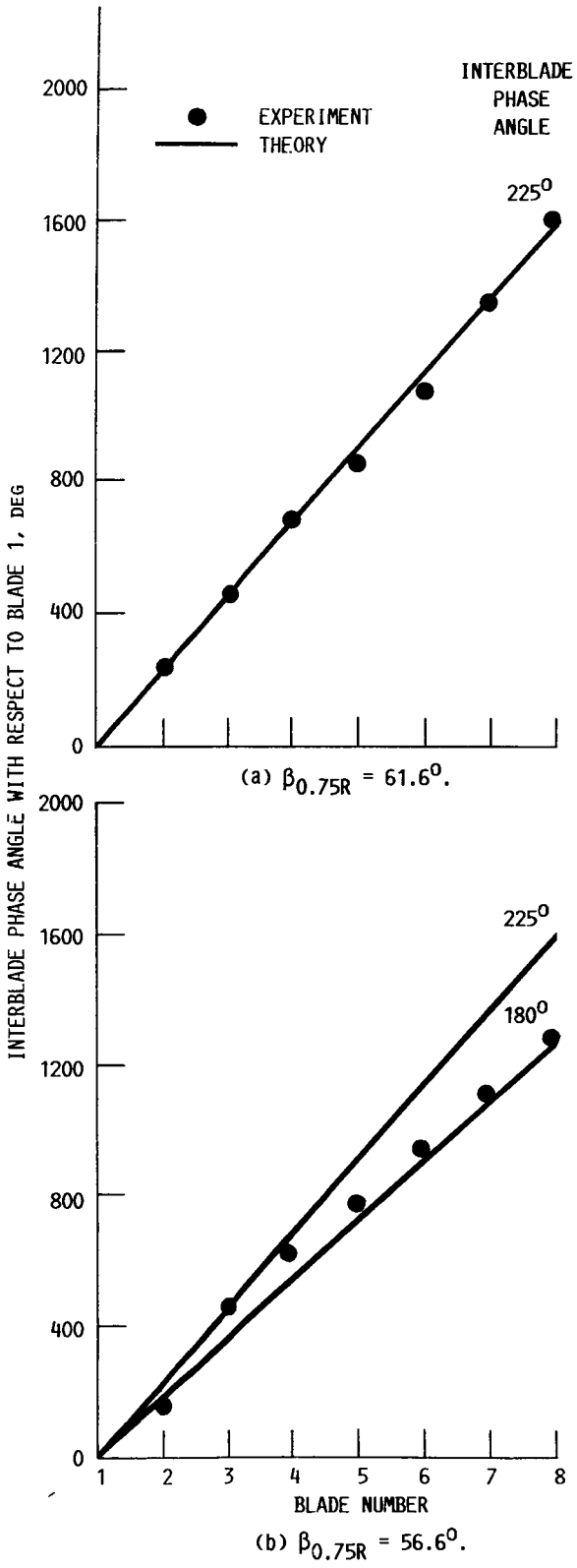

FIGURE 14. - COMPARISON OF MEASURED AND CALCULATED INTER-BLADE PHASE ANGLE AT FLUTTER, M = 0.55, Ω = 6950 RPM.

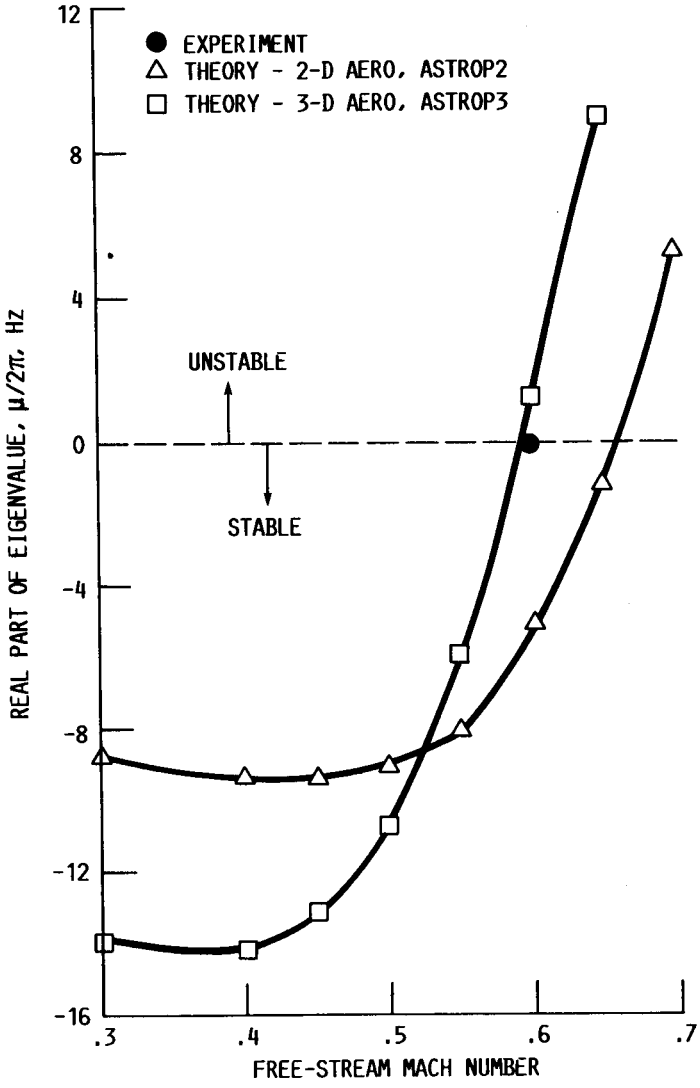

FIGURE 15.- COMPARISON OF 2-D AND 3-D UNSTEADY AERODYNAMIC THEORIES: Ω = 6080 RPM, $\beta_{0.75R} = 61.6^{0}$.

1. Report No.	2. Government Accession No.	3. Recipient's Catalog No.
NASA TM-88944 AIAA-87-0738		

4. Title and Subtitle	5. Report Date
Analytical Flutter Investigation of a Composite Propfan Model	
	6. Performing Organization Code 505-63-11

7. Author(s)	8. Performing Organization Report No.
K.R.V. Kaza, O. Mehmed, G.V. Narayanan, and D.V. Murthy	E-3392
	10. Work Unit No.

9. Performing Organization Name and Address	11. Contract or Grant No.
National Aeronautics and Space Administration Lewis Research Center Cleveland, Ohio 44135	
	13. Type of Report and Period Covered Technical Memorandum
12. Sponsoring Agency Name and Address	14. Sponsoring Agency Code
National Aeronautics and Space Administration Washington, D.C. 20546	

15. Supplementary Notes

Prepared for the 28th Structures, Structural Dynamics, and Materials Conference, cosponsored by the AIAA, ASME, AHS, and ASEE, Monterey, California, April 6-8, 1987. K.R.V. Kaza and O. Mehmed, NASA Lewis Research Center; G.V. Narayanan, Sverdrup Technology, Inc., Lewis Research Center, Cleveland, Ohio 44135; D.V. Murthy, The University of Toledo, Toledo, Ohio 43606 and NASA Resident Research Associate.

16. Abstract

This paper presents a theoretical model and an associated computer program for predicting subsonic bending-torsion flutter in propfans. The model is based on two-dimensional unsteady cascade strip theory and three-dimensional steady and unsteady lifting surface aerodynamic theory in conjunction with a finite element structural model for the blade. The analytical results compare well with published experimental data. Additional parametric studies are also presented illustrating the effects on flutter speed of steady aeroelastic deformations, blade setting angle, rotational speed, number of blades, structural damping, and number of modes.

17. Key Words (Suggested by Author(s))	18. Distribution Statement
Propfan; Flutter; Composites; Vibration; Aeroelasticity	Unclassified - unlimited STAR Category 39

19. Security Classif. (of this report)	20. Security Classif. (of this page)	21. No. of pages	22. Price*
Unclassified	Unclassified	23	A02

*For sale by the National Technical Information Service, Springfield, Virginia 22161